Creep behavior of an AlTiVNbZr$_{0.25}$ high entropy alloy at 1073 K

Petr Kral [a,*], Wolfgang Blum [b], Jiri Dvorak [a], Nikita Yurchenko [c], Nikita Stepanov [c], Sergey Zherebtsov [c], Lenka Kuncicka [a], Marie Kvapilova [a], Vaclav Sklenicka [a]

[a] *Institute of Physics of Materials, Czech Academy of Sciences, Zizkova 22, 616 62, Brno, Czech Republic*
[b] *Inst. f. Werkstoffwissenschaften, University of Erlangen-Nürnberg, D-91058, Erlangen, Germany*
[c] *Belgorod State University, Laboratory of Bulk Nanostructured Materials, Pobeda Str. 85, 308015, Belgorod, Russia*

ARTICLE INFO

ABSTRACT

The deformation behavior of an AlTiVNbZr$_{0.25}$ high entropy alloy at 1073 K was investigated in creep in protective argon atmosphere at stresses of 100–560 MPa with and without changes. In the initial condition after annealing at 1473 K for 24 h the alloys was composed of B2 matrix phase and coarse Zr$_5$Al$_3$-type particles. During creep a limited amount of new Nb$_2$Al-type sigma phase precipitates at the Zr$_5$Al$_3$/B2 hetero-phase interface and a quasi-stationary dislocation density of the expected order of magnitude are developed. The quasi-stationary creep rate obeys a three-power law and the transients after stress changes are inverted. This is interpreted in terms of the class A creep behavior with viscous glide due to cloud drag.

1. Introduction

Refractory high entropy alloys (RHEAs) form a new class of metallic alloys which are considered as promising structural materials for high-temperature applications [1]. They were introduced to satisfy the need for new alloys with temperature capacity beyond that of Ni-based superalloys – current materials of choice for demanding applications in aerospace industry and they can also possibly replace heavy alloys with W in certain applications [2,3]. There is no well-established definition of RHEAs, but generally it is believed that they should consist of nearly equiatomic mixtures of four to five refractory elements such as Hf, Mo, Nb, Ta. Other non-refractory elements may be used as well, for example, Al is frequently added to innovative alloys and composites to decrease density, and/or improve oxidation resistance [4,5].

The general idea behind the high entropy alloys was to produce solid solution structures, stabilized by high mixing entropy [6,7]. The firstly introduced RHEAs mostly featured single body centered cubic (bcc) structures [8,9]. However, as found later, RHEAs can be composed of multiple phases, including a B2, Laves phase, etc [1].

In terms of properties, RHEAs have already demonstrated remarkable specific strength at temperatures up to 1473 K, surpassing that of Ni-superalloys [1,10,11], while ductility of RHEAs still is generally too low for practical applications. Environmental resistance of some RHEAs is substantially better than that of conventional alloys based on refractory elements, yet this point should be investigated further [1,12,

13]. Significant efforts are undertaken these days to produce alloys with a balanced combination of high strength at elevated temperature, reasonable room temperature ductility, and good environmental resistance.

Yet other properties are also crucial for high-temperature applications [14]; one of them is creep resistance. Unfortunately, information about high-temperature creep behavior is available only for some high entropy alloys based on transition metals like Co, Cr, Fe, and Ni [15,16]. In this work we investigate the refractory alloy AlTiVNbZr$_{0.25}$. The present HEA alloy contains elements with optimal combination of high melting points and relatively low densities (such as Nb, Ti, V and Zr) and light weight metal Al. The elements such as Al, Nb, Ti, V have similar atomic radii and so they can form solid solution [17]. Previous experimental studies [11,17–19] showed that the elements predominantly influencing the strength of the current HEA alloy are Al and Zr. It was established that addition of Al frequently results in B2 ordering [18,20]. Formation of the B2 phase can have a strong positive effect on high temperature strength [18,21]. The addition of Zr causes the formation of secondary phases and the lattice distortions which may lead to the improvement of solid solution strengthening [18]. It was also found that the increase of Zr content reduces the long-range order parameter of the B2 matrix.

The present HEA alloy was chosen because similar AlTiVNbZr$_x$ – alloys already had shown good structural stability at 1073 K [19], and because AlTiVNbZr$_{0.25}$ has almost single B2-phase structure with a

significant amount of Zr_5Al_3-precipitates and a reasonable combination of high strength at temperatures up to 1073 K and room temperature ductility [18]. Preliminary results [18,19,22] showed that AlTiVNbZr$_x$ with B2 structure had a yield strength of about 680 MPa at 1073 K. This value exceeds that of other alloys with B2 structure such as NiAl [23,24], FeAl [25] and TiAl alloys [26]. The high temperature properties and deformation mechanisms of the present AlTiVNbZr$_x$ alloy have not been investigated yet. We present results on the compression creep behavior at constant as well as changed stress and on the microstructure before and after creep that indicate class A behavior at 1073 K.

2. Experimental materials and procedures

The alloy with nominal composition of AlNbTiVZr$_{0.25}$ was produced by arc melting of the high-purity (≥99.9 at.%) elements in argon atmosphere inside a water-cooled copper cavity. The produced ingot with dimensions of about $6 \times 15 \times 60$ mm^3 was re-melted five times. The measured chemical composition of the alloy (in at.%) was Al–22.8Nb–24.1Ti–23.5V-4.2Zr. After casting the alloy was air cooled and homogenized at 1473 K for 24 h in evacuated (10^{-2} Torr) quartz tubes filled with titanium chips.

Phase composition and microstructure of the alloy were studied using a scanning electron microscope (SEM, Tescan Lyra 3) and a transmission electron microscope (TEM, Jeol 2100F equipped with double tilt holder). Samples for SEM observations were prepared by mechanical polishing using oxide polishing suspension. TEM foils were prepared by grinding and subsequent argon ion milling (using PIPS II from Gatan). Phase identification in TEM was done by energy dispersive spectroscopy (EDS) and selective area electron diffraction (SAED).

Dislocation analysis was performed by two-beam Bragg-contrast imaging. Burgers vectors $\overline{b}$ of dislocations were deduced using the $\overline{g}.\overline{b} = 0$ criterion for dislocation invisibility [27] where $\overline{g}$ is the vector of the reflecting lattice planes. The mean dislocation densities ρ were evaluated from TEM micrographs with the interception method [28] as:

$$\rho = \frac{2N}{Lt_{\text{foil}}} \tag{1}$$

where N is number of the points of intersections between test lines and dislocation lines, L is the total length of test lines, and $t_{\text{foil}} \approx 0.2$ μm is the thickness of the TEM foil. TEM micrographs were taken under two beam conditions where most of the dislocations were visible in good contrast.

Uniaxial compression tests were conducted at 1073 K in argon gas atmosphere using cylindrical specimens with initial height $l_0 = 10$ mm and initial diameter of 5 mm, i.e., initial cross section $S_0 \approx 19.63$ mm^2. The true total compressive strain was determined as $|\ln(l/l_0)|$ where and l is the specimen height. The true inelastic compressive strain ε was determined by correcting for elastic strain contributions, coming mainly from the machine and from adjustment of the specimen to the compression machine in the beginning of deformation [29]. The uncertainty of the elastic correction is estimated to be usually distinctly less than 0.01. Two machines were used. Most tests were performed in a tensile creep machine equipped with a compression cage and a lever arm modifying the load F [30] such that the true stress $\sigma = F/S$, where $S=S_0 \exp(\varepsilon)$ is the specimen cross section, remains constant up to $\varepsilon \sim 0.3$. The stress change tests and tests with σ/MPa = 313, 315, 335, and 395 were performed without restriction in strain in a motor-driven machine (Zwick/Roell - Messphysik KAPPA LA) equipped with a control system. After creep the specimens were unloaded and cooled to room temperature (RT) for 6 h.

As the material parameters are not exactly known for the alloy, they were estimated by $M = 3$, the shear moduli estimated from the published results for different B2 structures, $G \approx 7 \times 10^{10}$ Pa [31,32], and $b = 2.9 \times 10^{-10}$ m [31]. The accuracy of these estimates is uncritical regarding the discussion of the results.

3. Experimental results

3.1. Microstructure before creep

Fig. 1 shows the microstructure of the alloy in the homogenized condition before creep. In accordance with a previous report [18] the experimental material is composed of B2 matrix and Zr_5Al_3 particles (Fig. 1). Intragranular particles were equiaxed and fine with mean size of about 1.55 μm. At the boundaries the particles were bigger and elongated and separated from the grain interior by a precipitate free zone. Image analysis led to an overall volume fraction of particles of about 8.5% and a volume fraction of boundary particles of 4.5%.

3.2. Creep behavior

The evolution of strain rate with strain is shown in Fig. 2. Tests at constant stress are shown in black, tests with stress changes in grey. For instance, the specimen crept at constant stress of 250 MPa (black) was cooled to room temperature test, and later subjected to a stress change test (grey). Branches of curves performed on the same specimen are connected by vertical lines. The inelastic strain accumulated during application of the creep load is rather small (<0.01). In several cases there is a pronounced relative minimum of $\dot{\varepsilon}$ at the beginning of creep. In the further course of creep the strain rate increases only slightly with strain at a small and gradually decreasing rate.

The curves measured at 200, 315 and 335 MPa have unusual shapes as the creep rate does not increase monotonically, but slightly decreases after initial increase. We believe that this is due to deviations from uniaxial compression. Such a deviation was evident from the post-creep shape of the specimen starting deformation at 315 MPa. The dashed lines with question marks indicate the probable course of creep at more uniaxial compression. However, negative influences of deviations from uniaxial compression appeared to be of minor importance compared to the usual scatter in creep tests.

The stress sensitivity of the creep rate at quasi-stationary (qs) dislocation structure was determined at $\varepsilon = 0.4$ by extrapolation (see Fig. 2). The triangle in Fig. 3 shows that the creep rate varies as:

$$\dot{\varepsilon} = B\sigma^{n_{qs}} \tag{2}$$

where B is a numerical constant and $n_{qs} = $ dlog $\dot{\varepsilon}$/dlogσ = 3 is the exponent of the creep rate in the qs range.

Fig. 4 shows one of the stress change tests in detail. The test covered
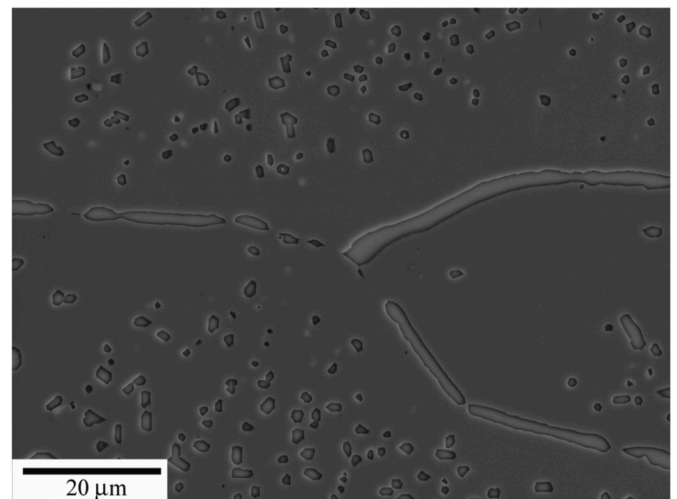

Fig. 1. Initial phase structure of AlNbTiVZr0.25 in homogenized condition before creep (SEM-BSE).
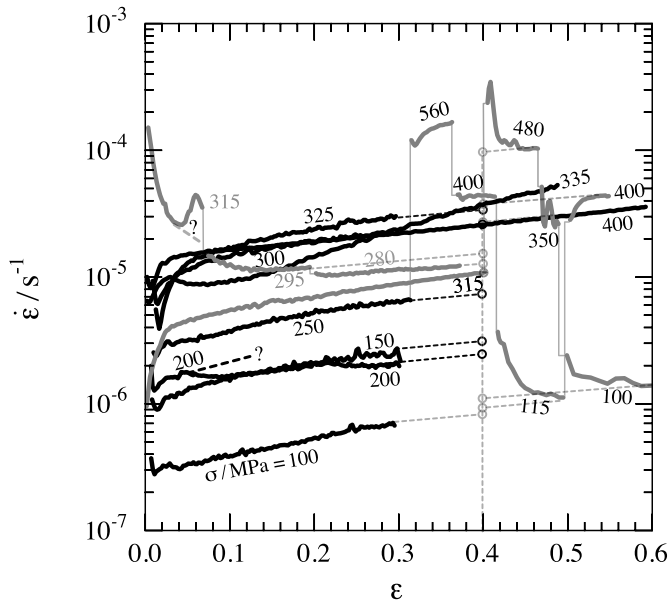
Fig. 2. The evolution of strain rate with strain; black: constant stress, grey: stress change tests; vertical lines connect tests on the same specimen; dashed extrapolation lines yield the quasi-stationary creep rates at $\varepsilon = 0.4$.
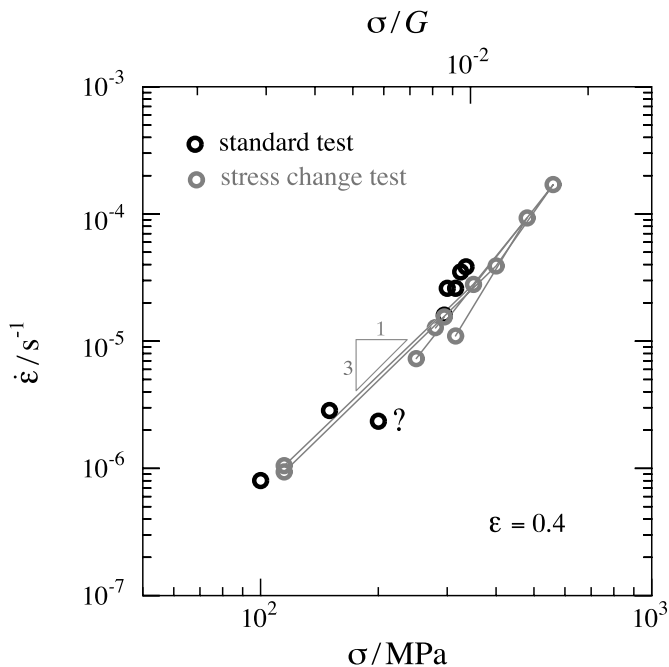

Fig. 3. Quasi-stationary creep rates at strain $\varepsilon = 0.4$ from Fig. 2 as function of stress. Data from stress change tests are connected by thin lines. Question mark refers to test at 200 MPa in Fig. 2.

the stress range from 560 MPa to 115 MPa and the creep rate varied over two decades. For technical reasons the applied stress had to be reduced to 50 MPa before the new stress could be applied. During this period the creep data could not be recorded. The change procedure took up to 50 s.

The most interesting result of this test is that large reduction of the stress from σ_2 to σ_3 causes a pronounced transient decline of the creep rate extending over a strain interval of 0.08.
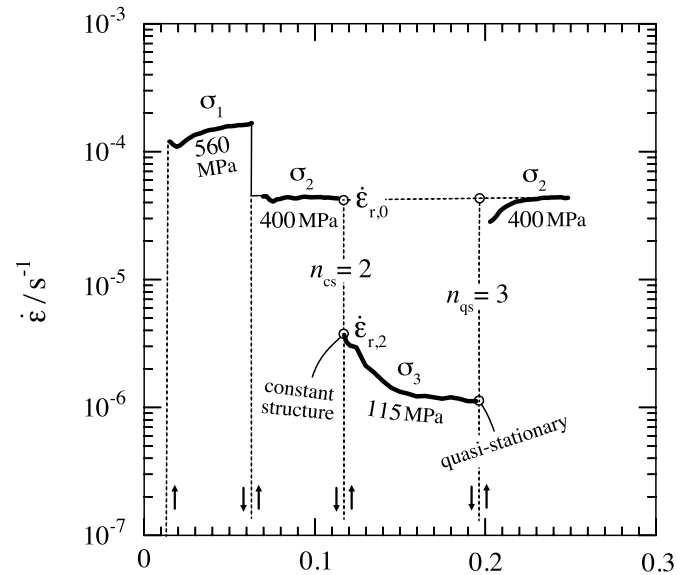

Fig. 4. Detailed view of stress change test following creep test from Fig. 2. Arrows indicate unloading and subsequent reloading to new stress (see text).

3.3. Microstructure after creep

Figs. 5 and 6 show the phase structure after creep. Selective area electron diffraction (SAED) (Fig. 7a) revealed that ordering of the B2 matrix (A in Fig. 5) is stable during medium-term creep testing at 1073 K (see caption of Fig. 5). Zr_5Al_3-particles (hexagonal with lattice parameters a = 0.8164 nm and c = 0.5702 nm [33]) appear in light grey (B in Fig. 5). Their nature was confirmed in TEM by EDS (Fig. 6b) and SAED (Fig. 6d). Zr_5Al_3 has 111/0001 crystallographic relationship to the B2 matrix (Fig. 6b). During creep the Zr_5Al_3-particles coarsened and increased in volume fraction compared to the initial state before creep. The mean size of intragranular Zr_5Al_3 particles was about 1.6 μm, the overall volume fraction of Zr_5Al_3 was about 10.8%, the volume fraction of boundary particles was about 6.5%, i.e., more than 60% of the Zr_5Al_3-volume was located at boundaries, similar to the initial state.

The mean hetero-phase interface spacing λ in the specimen tested at 100 MPa was ~6.8 μm. The stress necessary to overcome the particles by dislocations as per the Orowan by-pass is estimated by:
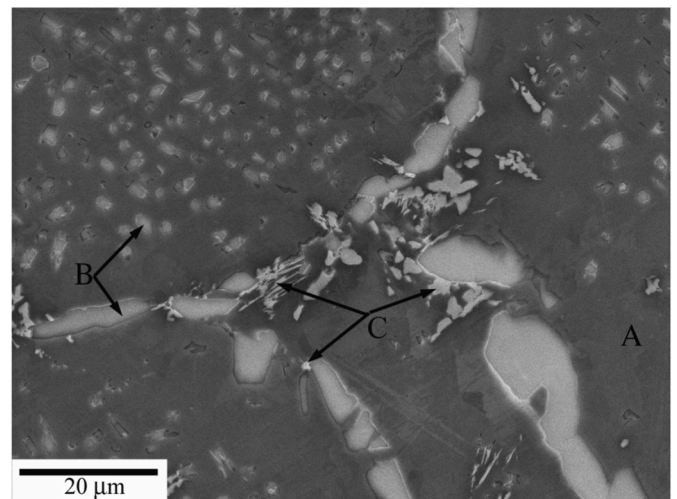

Fig. 5. Phase structure after creep testing at 100 MPa for about 185 h showing B2- matrix (A), Zr_5Al_3-particles (B), and secondary particles in bright white color (C).
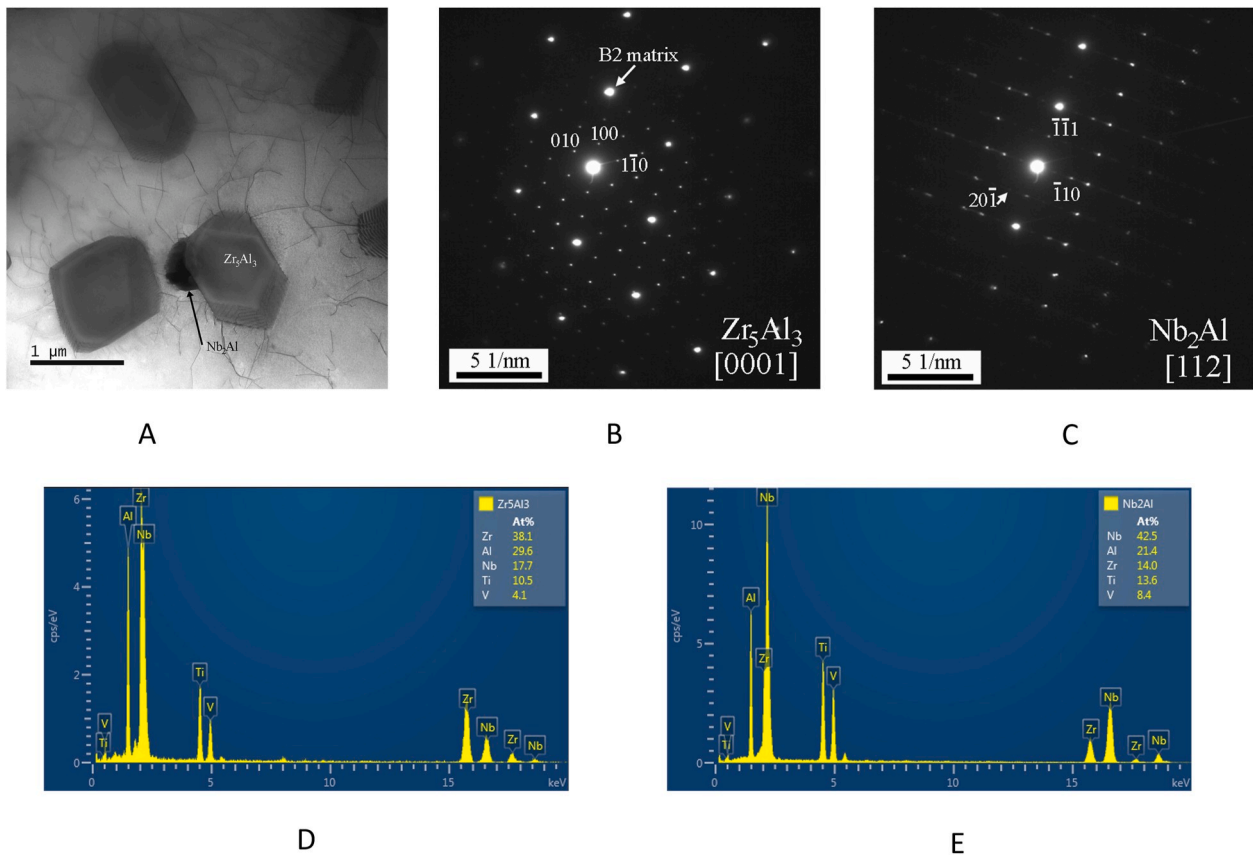
A

B

C

D

E

Fig. 6. Precipitates after creep at 100 MPa (see Fig. 2) for ~185 h: a) TEM view of B2-matrix with dislocations and precipitates of (grey) Zr_5Al_3- and secondary (black) Nb_2Al, b,c) SAED patterns of b) Zr_5Al_3 and c) Nb_2Al, d,e) chemical composition from EDS of d) Zr_5Al_3 and e) Nb_2Al.
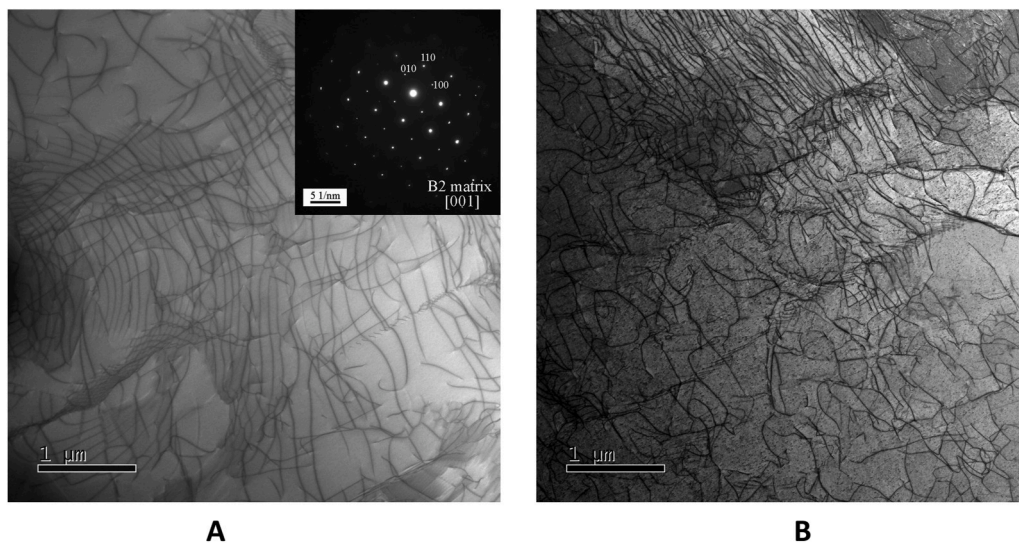

A

B

Fig. 7. Dislocation structure of the HEA tested at 1073 K and applied constant stress: a) 100 MPa, b) 325 MPa.

$$\sigma_{or} = M \frac{Gb}{\lambda} \qquad (3)$$

The result $\sigma_{or} \approx 8.9$ MPa suggests that Orowan stress is not high compared to the creep stresses applied in this work.

In addition to Zr_5Al_3 a new, secondary phase (marked C in Fig. 5) was observed after creep. It was found to be predominantly located at the interfaces between B2matrix and Zr_5Al_3-particles (Fig. 6a). Its volume fraction was about 2%. It predominantly contained Nb and Al (about 40

and 20 at.%, respectively). SAED analysis identified it as Nb_2Al type sigma phase (tetragonal phase with lattice parameters a = 0.9943 nm and c = 0.5186 nm [34]).

3.4. Dislocation structure after creep

Fig. 7a and b displays the dislocation structures after creep for a strain of about 0.3 at 100 MPa and 325 MPa, respectively (see Fig. 2).

The dislocations are randomly distributed and slightly curved. Low-angle boundaries form at the incipient stage, however there is no well-established subgrain structure yet.

Fig. 8 shows dislocations after creep at 100 MPa (a - d) and 325 MPa (e − h) under different Bragg conditions. The results demonstrate (Fig. 8 a-d) that some dislocations are visible for $\bar{g} = \bar{1}10, \ 110$ and $0\bar{2}0$, but completely invisible for $\bar{g} = 200$. So these dislocations have the Burgers vector of a type other than $a_0<111>$ that is generally expected in BCC materials.

The dislocations that are invisible for $\bar{g} = 200$ may be dislocations of the $a_0<011>$ or $a_0<010>$ type. These dislocations are relatively long and less strongly curved than the other dislocations. Many of the dislocation segments have a Burgers vector of the $a_0<111>$ type. The long weakly curved dislocations can be observed also in microstructure tested at 325 MPa (Fig. 8 e-h). These dislocations are invisible for $\bar{g} = 0\bar{1}1$ and $\bar{g} = 0\bar{2}0$ (Fig. 8 e-h). It means that these dislocations have the Burgers vector of type $a_0<100>$. However, most of the dislocation segments have Burgers vector of type $a_0<111>$.

The dislocation density ρ given here include dislocations with sharp contrast lying at boundaries, but not the dense, unresolvable dislocation network of the boundaries themselves. The dislocation density ρ is larger at the higher stress. Fig. 9 gives the average dislocation spacing $\rho^{-0.5}$ as a function of stress. Error bars represents maximal and minimal measured dislocation densities in microstructures tested at 100 and 325 MPa (Fig. 8). The lowest dislocation density ($\rho \approx 2.2 \ 10^{13}$ m^{-2}) was measured at 100 MPa for diffracting vector $\bar{g} = 200$. The highest dislocation density ($\rho \approx 9.2 \ 10^{13}$ m^{-2}) was measured at 325 MPa for vector $\bar{g} = 0\bar{1}1$.

The reference line $\rho = bG/\sigma$ in Fig. 9 has a simple meaning. In deformation of pure materials the resolved shear stress $\tau = \sigma/M$ is related to the dislocation density by $\tau = \alpha Gb\rho^{0.5}$ (Taylor formula) where $\alpha \approx 0.3$. It is known that the flow stress σ is close to the athermal stress component σ_G, because the thermal stress component $\sigma^* = \sigma - \sigma_G$ driving dislocations over thermally activatable obstacles is comparatively small. As M ≈ 3, $\sigma_G \approx bG/\sigma$. This means that the arrows in Fig. 9 represent the
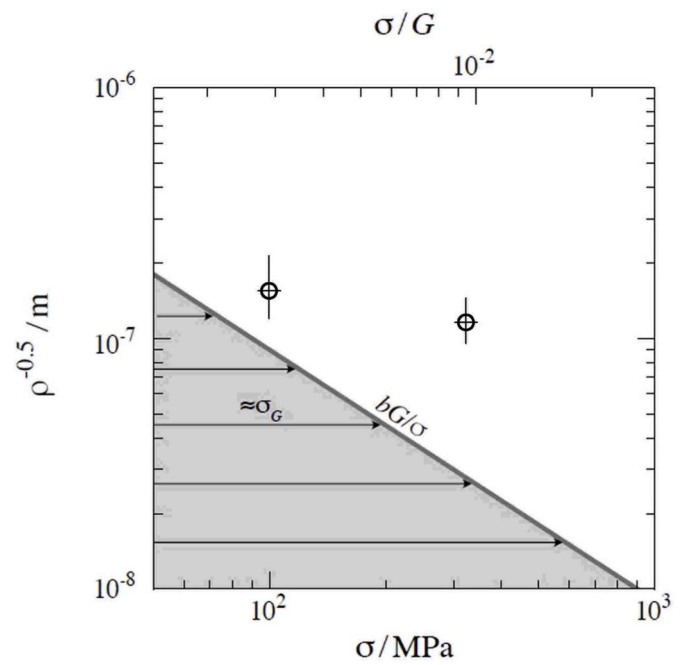

Fig. 9. Mean dislocation spacing (Fig. 8) as a function of stress; arrows mark $\sigma_G \approx bG\rho^{0.5}$ for given ρ.

athermal stress component. The experimental stresses at given ρ lie right of the reference line. This will be discussed below in terms of solid solution strengthening causing a relatively large value of σ^* for motion of dislocations.
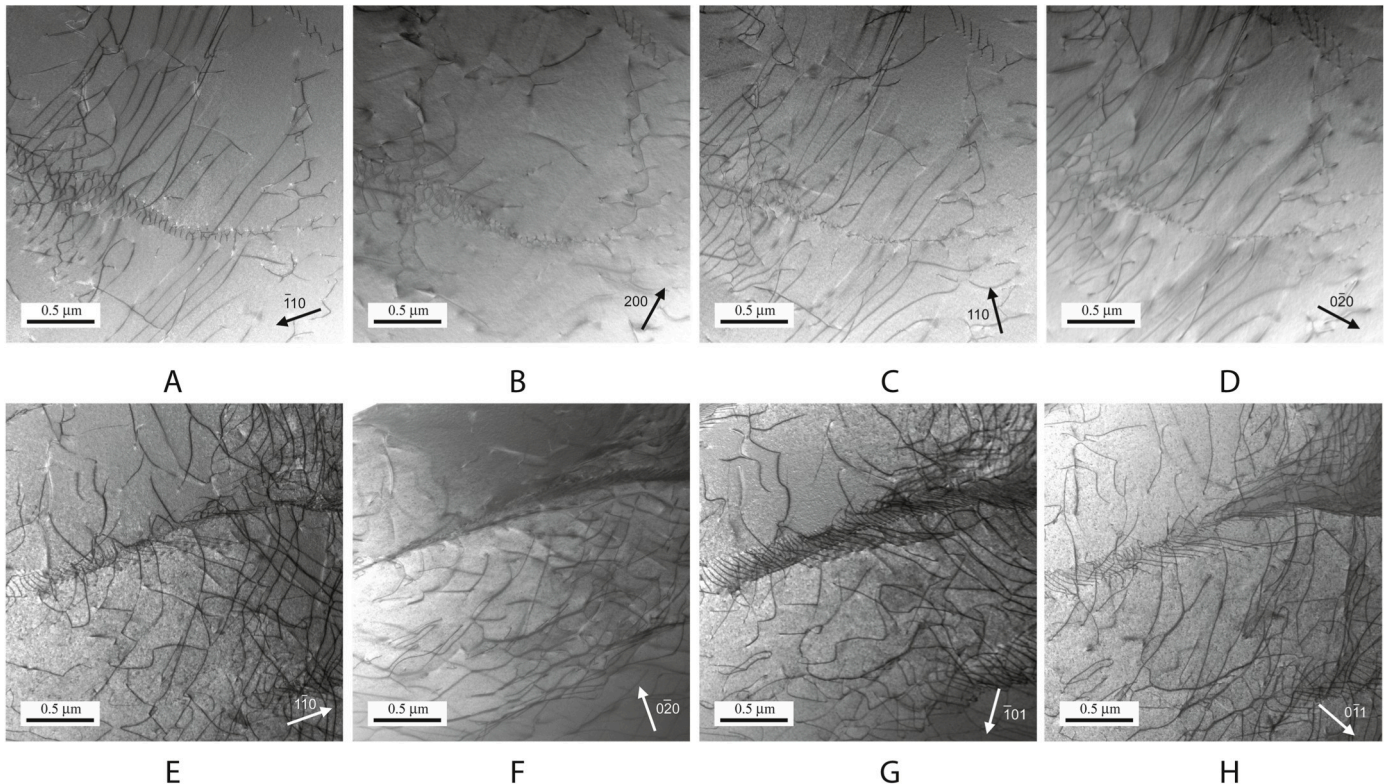

Fig. 8. Dislocation structure of the investigated HEA tested at 1073 K and a) – d) 100 MPa, zone axis near [001], e) – h) 325 MPa, zone axis near [111].

4. Discussion

Although the phase structures of HEAs have been assumed to be very stable due to the effects of high entropy and slow diffusion [4], it was revealed that many alloys with a stable single-phase structure decompose at high temperatures into a complex mixture of different phases upon annealing at lower temperature [35–39]. Annealing under stress (as in creep) is expected to result in even more pronounced decomposition. However, the phase structure of the investigated AlNbTiVZr$_{0.25}$ alloy was found to be relatively stable during creep testing at 1073 K. The main constitutive phases (the B2 matrix and coarse Zr$_5$Al$_3$ type particles) and a small amount of the Nb$_2$Al type phase were observed in the specimens after creep. Good structural stability of the AlNbTiVZr$_x$ (x = 0.5–1.5) alloys during annealing for 100 h at 1073K was attributed to the fact that Al, as the main second-phase forming element in the Al–Nb–Ti–V–Zr system, has already been partitioned to the Zr$_5$Al$_3$-type particles during homogenization at 1473 K [18,19].

However, the formation of the Nb$_2$Al type phase during creep deserves additional analysis. The appearance of these particles at the B2/Zr$_5$Al$_3$ hetero-phase interface, i.e. places with the lowest nucleation barrier, suggests that their nucleation of this phase is difficult. Most probably, this is due to low driving force for sigma phase formation in the examined alloy, which agrees with the small fraction of the phase even after testing for 185 h. Note that a high amount of a similar Nb$_2$Al-type phase appeared in a quaternary AlNbTiV alloy after annealing at 1073 K [19]. The comparison between the quaternary and the examined alloy confirms that even a relatively small amount of Zr (4.2 at.%) almost completely prevents the formation of sigma phase. Despite the presence of precipitates within the grains and at the boundaries, the investigated HEA alloys exhibits creep behavior similar to a solid solution. It may be explained by the lower strength of particles at the creep temperature in comparison with B2 matrix. It should be noted that the precipitates (Figs. 1 and 5) were observed at room temperature and the volume fraction of precipitates at the testing temperature can be different. The specimens after creep exhibited a good ductility and the formation of cavities and cracks along boundaries was not observed.

Regardless of the slight softening effect, the material appears to enter a quasi-stationary state where strengthening and softening mechanisms balance each other so that strength remains nearly constant at constant deformation conditions. There are arguments that the present material belongs to the class A (alloy class) [40,41]. In this class the interaction of dislocations and solute atoms plays a decisive role. In HEAs there are a lot of different atoms which induce a multitude of possible interactions with dislocations. These induce formation of a cloud, i.e. an atomic configuration around the dislocations where specific atoms are enriched compared to others. To move under stress the dislocations either have to break away from the clouds or they need to drag the cloud along with them. This requires a strongly rate-dependent thermal (drag) stress component $\sigma^* = \sigma - \sigma_G$. The observed $n_{qs} = 3$ is characteristic for class A behavior with viscous motion of cloud-bearing dislocations [42]. Fig. 9 shows that the experimental stresses at given ρ lie at the right of the reference line bG/σ marking the athermal stress component σ_G. This means that at given ρ the applied stress sigma is larger than the σ_G-estimate, consistent with a non-negligible thermal stress component σ^*. The sluggish formation of subgrains observed in this work (Figs. 7 and 8) is another characteristic of class A behavior. Finally we mention that the viscous glide of cloud-bearing dislocations encourages glide on unusual slip systems that are usually difficult to activate. This is consistent with the observation of dislocations with different Burgers vectors (not only <111>) in the present work (see above) and in Al–5Mg [43] and in the B2-type Fe–40%Al alloy where the formation of <100> and <111> dislocation segments led to an increase in flow stress and work hardening rate [44].

Based on class A behavior in the investigated range we envisage that cloud drag allows the dislocations move viscously at a velocity controlled by diffusion. Dislocations of opposite signs approaching each other get captured in dipolar configurations (Fig. 10a). Local annihilation of the dipoles leads to coalescence of the areas across which the dislocations have slipped (Fig. 10b). Thereby dislocation segments with negative curvature are generated (Fig. 10c). Expansion of dislocation loop segments with positive curvature *increases* the dislocation density ρ (Fig. 10a), local dipole annihilation (Fig. 10b) followed by shrinking of loop segments with negative curvature *decreases* ρ (Fig. 10c).

Within the picture of cloud drag the transient behavior in the beginning of creep (Fig. 2) and after stress changes can be understood. When an abrupt change of stress disturbs the balance of generation and annihilation, a new balance corresponding to the new stress needs to be established. Qualitatively, the dislocation density ρ scales with stress. An increase in stress leads to a net increase in ρ (decrease in spacing $\rho^{-0.5}$) and vice versa [45]. The dislocation velocity also changes, oppositely to the density. Due to cloud drag the stress-induced changes in velocity may be weaker than the changes in ρ. In this case the transients become opposite to the ones observed in pure materials (inverted transients, see e.g. Ref. [42,45]). In any case, the transients are strongly damped compared to pure materials.

However, this qualitative reasoning does not fully explain the pronounced inverted transient after a large stress reduction of the kind following the change in Fig. 4 from σ_2 to $\sigma_{3=}\sigma_2R$ with R = 0.29.

Fig. 11 shows a schematic of the evolution of ρ in response to the stress σ in this test. After the large stress reduction to $R\sigma$ the thermal stress component is expected to be negative. That should prompt back flow and subsequent standstill of the dislocations for a period long enough to make σ^* positive again by recovery. In the present tests the strain during unloading has not been monitored. Exact measurements on Al–5Mg in the temperature range of viscous dislocation motion showed back flow to set in for R < 0.5 [45,46]. However, after relaxation of the internal stresses the rate turned positive again and reached a relative maximum $\dot{\varepsilon}_{r,2}$. The dashed band of $\dot{\varepsilon}_{r,2}$ data in Fig. 12 extends down to R = 0.15. An extended period of standstill ('incubation period') was not observed. The so-called constant structure stress exponent $n$cs of $\dot{\varepsilon}_{r,2}$ is close to 2 while the line with $n$qs = 3 represents the qs state. The large circle comes from our change test (Fig. 4) and is in good agreement with the grey data band for Al–5Mg.

The similarity to the class M alloy Al–5Mg is obvious. Weckert and Blum [45] concluded that the conventional σ^*- model used in the preceding text is insufficient and must be supplemented by recovery strain, i.e. strain associated with dynamic recovery of dislocations, an example of which is sketched in Fig. 10c. This means that the strain rate $\dot{\varepsilon}$ is a sum of two terms:

$$\dot{\varepsilon} = \dot{\varepsilon}^+ + \dot{\varepsilon}^- \tag{4}$$

here $\dot{\varepsilon}^+$ is the strain rate due to glide of dislocations under a thermal stress component $\sigma^{*+} = \sigma - \sigma_G^+$ with $\sigma_G \propto \rho^{0.5}$ and related with dislocation storage, while $\dot{\varepsilon}^-$ is the strain rate associated with dynamic recovery at a thermal stress component σ^{*-}. So far relatively little is known about $\dot{\varepsilon}^-$.
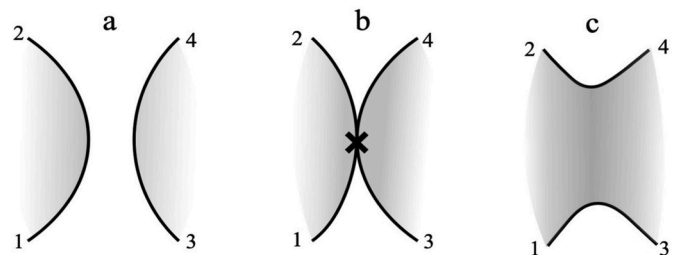

Fig. 10. Scheme of dynamic recovery: a) positively curved dislocation segments (1,2) and (3,4) expand during growth of slipped areas (shaded), b) coagulation of slipped areas by dipole capture and annihilation at X, c) negatively curved dislocation segments (1,3) and (2,4) shrink during growth of slipped area. Note that (1,2) and (3,4) in general lie in different slip planes.
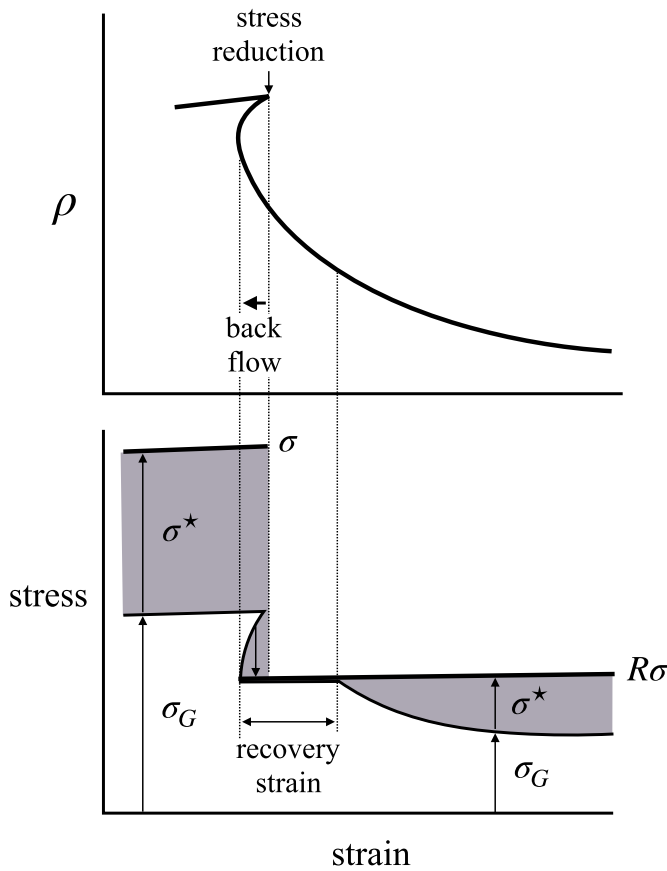
Fig. 11. Scheme of variation of dislocation density ρ and thermal stress component σ^* (shaded) with strain in test with large stress reduction from σ to $R\sigma$; in period of $\sigma^* \leq 0$ strain is associated with dynamic recovery (see Eq. (4)).
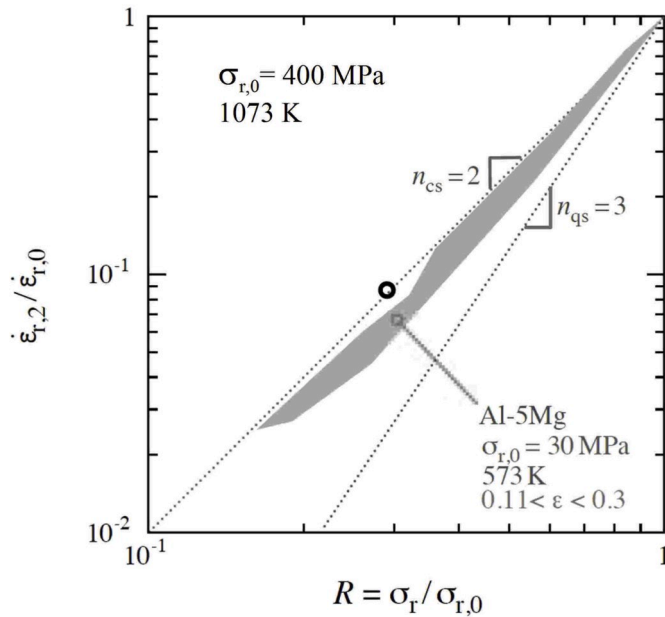

Fig. 12. Constant structure creep rate $\dot{\varepsilon}_{r,2}$ from Fig. 4 in rate-stress field normalized by $\sigma_{r,0} = \sigma_2$ and $\dot{\varepsilon}_{r,0}$; with data for class M alloy Al–Mg [46] for comparison.

In class A materials the situation is relatively simple insofar as all the

dislocations move in a viscous manner, those moving against obstacles as well as those being attracted to recovery sites. So Blum and Weckert [45] suggested to neglect the kinetic differences between the two terms $\dot{\varepsilon}^+$ and $\dot{\varepsilon}^-$ and lump them together in the Orowan equation:

$$\dot{\varepsilon} = (b/M)\rho \, \nu \, \sigma^*, \qquad \nu \propto \sigma^* \qquad (5)$$

where ρ is the total density of free dislocations and σ^* is given by a wide distribution of "effective" stresses σ^* for viscous glide with low values of σ^* when athermal obstacles oppose dislocation glide (Fig. 10a) and high values of σ^* when recovery processes support the viscous motion (as e.g. in Fig. 10c). As shown in Appendix A an equal distribution of σ^* in the interval from 0 to σ leads to a constant structure stress exponent $n_{cs} = 2$ [45] and a qs stress exponent $n_{qs} = 3$ as measured. This shows that the model of dislocation glide under distributed effective stresses in presence of recovery strain is capable of fitting the observed results.

5. Conclusions

The initial structure of the AlTiVNbZr$_{0.25}$ alloy (annealed at 1473 K for 24 h) was composed of the B2 matrix phase with coarse Zr$_5$Al$_3$ phase particles. Creep testing at 1073 K led to formation of precipitates of Nb$_2$Al type sigma phase. The new phase was predominantly located at Zr$_5$Al$_3$/B2 hetero-phase interface boundaries.

The creep characteristics are typical for class A behavior with viscous glide by interaction of dislocations and specific atoms. The quasi-stationary creep rate varies according to a three-power-law, the transients are inverted. The behavior of the present HEA agrees quantitatively with that of the prototypical class M alloy Al–Mg. After large stress reductions creep associated with dynamic recovery dominates.

Declaration of competing interest

The authors declare that they have no known competing financial interests or personal relationships that could have appeared to influence the work reported in this paper.

CRediT authorship contribution statement

Petr Kral: Conceptualization, Methodology, Validation, Formal analysis, Investigation, Resources, Data curation, Writing - original draft, Writing - review & editing, Visualization, Supervision. **Wolfgang Blum:** Conceptualization, Methodology, Formal analysis, Data curation, Writing - original draft, Writing - review & editing, Visualization, Supervision. **Jiri Dvorak:** Methodology, Validation, Investigation, Resources, Data curation, Visualization. **Nikita Yurchenko:** Methodology, Investigation, Resources, Writing - original draft. **Nikita Stepanov:** Methodology, Investigation, Resources, Writing - original draft. **Sergey Zherebtsov:** Conceptualization, Investigation, Resources, Writing - original draft, Supervision. **Lenka Kuncicka:** Methodology, Investigation, Visualization. **Marie Kvapilova:** Methodology, Investigation, Visualization. **Vaclav Sklenicka:** Methodology, Investigation, Supervision.

Acknowledgement

A. Appendix. Model of viscous flow in presence of dynamic recovery

$f\rho(\sigma'_G, \sigma)$ be the frequency $d\rho/d\sigma'_G$ of dislocation segments $d\rho$ sensing a local value σ'_G of athermal stress component in the qs state at stress σ. Local storage of dislocations occurs where high internal stresses oppose dislocation motion by high σ_G. Local dynamic recovery of dislocations occurs where short-and long-range internal stresses from dislocation interactions reduce σ'_G. Viscous motion of dislocations is driven by the local thermal stress component

$$\sigma^{*'} = \sigma - \sigma'_G. \tag{6}$$

Fig. 13a describes the quasi-stationary state at a given stress σ. We assume $f_\rho(\sigma'_G, \sigma)$ to be constant at constant σ equal to $\widehat{f}_\rho(\sigma)$ in the interval $0 \leq \sigma'_G \leq \sigma$ and zero outside. The area under the distribution curve represents the qs dislocation density at stress σ:

$$\rho_{qs}(\sigma) = \int_{\sigma'_G} f_\rho(\sigma'_G, \sigma) d\sigma'_G \qquad\qquad \sigma = constant \tag{7}$$

$$= \int_0^\sigma \widehat{f}_\rho(\sigma) d\sigma'_G \tag{8}$$

$$= \widehat{f}_\rho(\sigma)\sigma. \tag{9}$$

We assume that the amplitude $\widehat{f}_\rho(\sigma)$ scales with σ as

$$\widehat{f}_\rho(\sigma) = f_{qs}\frac{\sigma}{(Gb)^2} \qquad\qquad f_{qs} \approx 1 \tag{10}$$

Insertion to Eq. (9) yields

$$\rho_{qs}(\sigma) = f_{qs}\left(\frac{\sigma}{Gb}\right)^2 \tag{11}$$

in agreement with the Taylor relation; this approximation suffices for the present purpose. In consequence of Eq. (6), σ'_G - distribution $f_\rho(\sigma^{*'}, \sigma)$ (Fig. 13b) of ρ-segments is identical to the σ'_G - distribution $f_\rho(\sigma'_G, \sigma)$ (Fig. 13a).

After describing the qs state, we now consider an (ideally) sudden reduction of stress from σ to $R\sigma$. The distribution of local σ'_G remains nearly unaffected, because it is bound to the existing dislocation structure developed in the qs state before the relative stress reduction to R< 1. By contrast, the stress reduction immediately diminishes the local values of the thermal stress component $\sigma^{*'}$ and its distribution to the left (Fig. 13c). Thus part of the local $\sigma^{*'}$- values becomes negative (Fig. 13c). The negative $\sigma^{*'}$ -values cause local anelastic back flow. Thereby athermal stresses σ'_G get relaxed, until the negative values of σ^* have gone to zero (Fig. 13d). The so immobilized dislocations form a sharp cusp in the distribution at $\sigma^* = 0$ in Fig. 13d, indicated by the arrow at $\sigma^* = 0$ pointing upward. The dislocations with still positive $\sigma^{*'}$ continue to move. We assume that the motion occurs viscously at a local velocity of

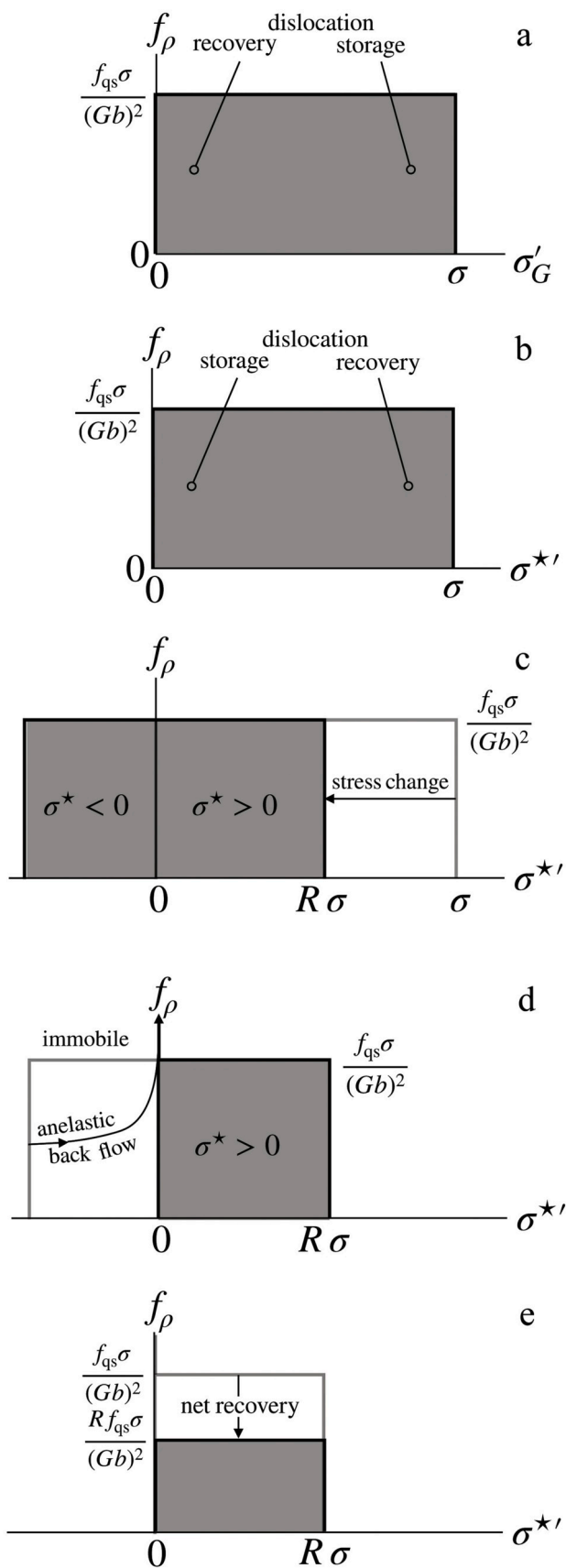$$v = A \cdot \sigma^{*'} \qquad\qquad A = constant \tag{12}$$

Fig. 13. Frequency distribution of athermal and thermal stress components σ'_G and $\sigma^{\star\prime}$ in stress reduction test (see text): a) σ'_G in qs state before change of stress to relative stress R, b) $\sigma^{\star\prime}$ in qs state before change of stress, c) just after sudden R-reduction, d) after anelastic back flow with partial relaxation of back stresses, e) after dynamic recovery to new qs state at $R\sigma$.

during glide as well as during recovery, as both processes are diffusion-controlled. According to the Orowan equation each differential dislocation density $d\rho = f_\rho(\sigma^{*\prime}, \sigma)d\sigma^{*\prime}$ contributes to the strain rate by $d\dot{\varepsilon} = (b/M)d\rho v(\sigma^{*\prime})$ in the strain interval $0 \leq \sigma^{*\prime} \leq R\sigma$, so that the strain rate results as:

$$\varepsilon = \frac{b}{M} \int v(\sigma^{*}) f_\rho(\sigma^{*}, \sigma) d\sigma^{*} \tag{13}$$

In the 'constant structure' situation of Fig. 13d, after anelastic back flow due to stress reduction to $R\sigma$, but with negligible dynamic recovery since the stress reduction, $\widehat{f}_\rho$ is the same as it was before at σ (Eq. (10)).

Combining Eqs. (10), (12) and (13), the strain rate $\dot{\varepsilon}_{r,2}$ at constant structure results as:

$$\dot{\varepsilon}_{\text{r,2}} = \frac{b}{M} A \frac{f_{qs} \sigma}{(Gb)^2} \int_0^{R\sigma} \sigma^* d\sigma^* = B \sigma^3 R^2 \tag{14}$$

$$B = \frac{bA\widehat{f}_{\text{qs}}}{2 M (Gb)^2} \tag{15}$$

For R = 1, i.e. no stress reduction, $\dot{\varepsilon}_{r,2}$ is identical to the qs strain rate

$$\dot{\varepsilon}_{\text{qs}}(\sigma) = B\sigma^{n_{qs}} \qquad n_{\text{qs}} = 3, \tag{16}$$

obeying a three-power law, and the 'constant structure' rate $\dot{\varepsilon}_{cs} \approx \dot{\varepsilon}_{r,2}$ after qs deformation varies with the second power of stress or R, respectively:

$$\dot{\varepsilon}_{\text{cs}}(R\sigma) = \dot{\varepsilon}_{\text{qs}} R^{n_{cs}} \qquad n_{\text{cs}} = 2 \tag{17}$$

The transient from the qs rate $\dot{\varepsilon}_{\text{qs}}(\sigma)$ at σ to the qs rate $\dot{\varepsilon}_{\text{qs}}(R\sigma)$ at reduced stress $R\sigma$ results from net dynamic recovery of the density of dislocations given by the decrease of $\widehat{f}_\rho$ in Fig. 13e by the factor R to the new qs level at reduced stress $R\sigma$.

References

[1] O.N. Senkov, D.B. Miracle, K.J. Chaput, J.-P. Couzinie, Development and exploration of refractory high entropy alloys—a review, J. Mater. Res. 33 (2018) 3092–3128, https://doi.org/10.1557/jmr.2018.153.

[2] L. Kunčická, R. Kocich, Ch Hervoches, A. Macháčková, Study of structure and residual stresses in cold rotary swaged tungsten heavy alloy, Mater. Sci. Eng. A 704 (2017) 25–31, https://doi.org/10.1016/j.msea.2017.07.096.

[3] R. Kocich, L. Kunčická, D. Dohnalík, A. Macháčková, M. Šofer, Cold rotary swaging of a tungsten heavy alloy: numerical and experimental investigations, Int. J. Refract. Met. H 61 (2016) 264–272, https://doi.org/10.1016/j.ijrmhm.2016.10.005.

[4] O.N. Senkov, S.V. Senkova, C.F. Woodward, Effect of aluminum on the microstructure and properties of two refractory high-entropy alloys, Acta Mater. 68 (2014) 214–228, https://doi.org/10.1016/j.actamat.2014.01.029.

[5] H. Chen, A. Kauffmann, B. Gorr, D. Schliephake, C. Seemüller, J.N.N. Wagner, H.-J. Christ, M. Heilmaier, Microstructure and mechanical properties at elevated temperatures of a new Al-containing refractory high-entropy alloy Nb-Mo-Cr-Ti-Al, J. Alloys Compd. 661 (2016) 206–215, https://doi.org/10.1016/j.jallcom.2015.11.050.

[6] J.-W. Yeh, S.-K. Chen, S.-J. Lin, J.-Y. Gan, T.-S. Chin, T.-T. Shun, C.-H. Tsau, S.-Y. Chang, Nanostructured high-entropy alloys with multiple principal elements: novel alloy design concepts and outcomes, Adv. Eng. Mater. 6 (2004) 299–303, https://doi.org/10.1002/adem.200300567.

[7] D.B. Miracle, O.N. Senkov, A critical review of high entropy alloys and related concepts, Acta Mater. 122 (2017) 448–511, https://doi.org/10.1016/j.actamat.2016.08.081.

[8] O.N. Senkov, G.B. Wilks, D.B. Miracle, C.P. Chuang, P.K. Liaw, Refractory high-entropy alloys, Intermetallics 18 (2010) 1758–1765, https://doi.org/10.1016/j.intermet.2010.05.014.

[9] O.N. Senkov, J.M. Scott, S.V. Senkova, D.B. Miracle, C.F. Woodward, Microstructure and room temperature properties of a high-entropy TaNbHfZrTi alloy, J. Alloys Compd. 509 (2011) 6043–6048, https://doi.org/10.1016/j.jallcom.2011.02.171.

[10] O.N. Senkov, C. Woodward, D.B. Miracle, Microstructure and properties of aluminum-containing refractory high-entropy alloys, J. Occup. Med. 66 (2014) 2030–2042, https://doi.org/10.1007/s11837-014-1066-0.

[11] N.Y. Yurchenko, N.D. Stepanov, D.G. Shaysultanov, M.A. Tikhonovsky, G. A. Salishchev, Effect of Al content on structure and mechanical properties of the AlxCrNbTiVZr (x = 0; 0.25; 0.5; 1) high-entropy alloys, Mater. Char. 121 (2016) 125–134, https://doi.org/10.1016/j.matchar.2016.09.039.

[12] T.M. Butler, K.J. Chaput, Native oxidation resistance of Al20Nb30Ta10Ti30Zr10 refractory complex concentrated alloy (RCCA), J. Alloys Compd. 787 (2019) 606–617, https://doi.org/10.1016/J.JALLCOM.2019.02.128.

[13] B. Gorr, M. Azim, H.J. Christ, T. Mueller, D. Schliephake, M. Heilmaier, Phase equilibria, microstructure, and high temperature oxidation resistance of novel refractory high-entropy alloys, J. Alloys Compd. 624 (2015) 270–278, https://doi.org/10.1016/j.jallcom.2014.11.012.

[14] L. Kunčická, A. Macháčková, N.P. Lavery, R. Kocich, J.C.T. Cullen, L.M. Hlaváč, Effect of thermomechanical processing via rotary swaging on properties and residual stress within tungsten heavy alloy, Int. J. Refract. Met. H 87 (2019), 105120, https://doi.org/10.1016/j.ijrmhm.2019.105120.

[15] T. Cao, J. Shang, J. Zhao, C. Cheng, R. Wang, H. Wang, The influence of Al elements on the structure and the creep behavior of AlxCoCrFeNi high entropy alloys, Mater. Lett. 164 (2016) 344–347, https://doi.org/10.1016/J.MATLET.2015.11.016.

[16] T.-K. Tsao, A.-C. Yeh, C.-M. Kuo, K. Kakehi, H. Murakami, J.-W. Yeh, S.-R. Jian, The high temperature tensile and creep behaviors of high entropy superalloy, Sci. Rep. 7 (2017) 12658, https://doi.org/10.1038/s41598-017-13026-7.

[17] N.D. Stepanov, D.G. Shaysultanov, G.A. Salishchev, M.A. Tikhonovsky, Structure and mechanical properties of a light-weight AlNbTiV high entropy alloy, Mater. Lett. 142 (2015) 153–155, https://doi.org/10.1016/j.matlet.2014.11.162.

[18] N.Y. Yurchenko, N.D. Stepanov, S.V. Zherebtsov, M.A. Tikhonovsky, G. A. Salishchev, Structure and mechanical properties of B2 ordered refractory AlNbTiVZrx (x = 0–1.5) high-entropy alloys, Mater. Sci. Eng. A 704 (2017) 82–90, https://doi.org/10.1016/j.msea.2017.08.019.

[19] N.Y. Yurchenko, N.D. Stepanov, A.O. Gridneva, M.V. Mishunin, G.A. Salishchev, S. V. Zherebtsov, Effect of Cr and Zr on phase stability of refractory Al-Cr-Nb-Ti-V-Zr high-entropy alloys, J. Alloys Compd. 757 (2018) 403–414, https://doi.org/10.1016/j.jallcom.2018.05.099.

[20] H. Chen, A. Kauffmann, S. Seils, T. Boll, C.H. Liebscher, I. Harding, K.S. Kumar, D. V. Szabó, S. Schlabach, S. Kauffmann-Weiss, F. Müller, B. Gorr, H.-J. Christ, M. Heilmaier, Crystallographic ordering in a series of Al-containing refractory high entropy alloys Ta-Nb-Mo-Cr-Ti-Al, Acta Mater. 176 (2019) 123–133, https://doi.org/10.1016/J.ACTAMAT.2019.07.001.

[21] O.N. Senkov, D. Isheim, D.N. Seidman, A.L. Pilchak, Development of a refractory high entropy superalloy, Entropy 18 (2016) 102, https://doi.org/10.3390/e18030102.

[22] N.D. Stepanov, N. Yu Yurchenko, V.S. Sokolovsky, M.A. Tikhonovsky, G. A. Salishchev, An AlNbTiVZr0.5 high-entropy alloy combining high specific strength and good duktility, Mater. Lett. 161 (2015) 136–139, https://doi.org/10.1016/j.matlet.2015.08.099.

[23] J.D. Whittenberger, R.D. Noebe, C.L. Cullers, K.S. Kumar, S.K. Mannan, 1000 to 1200 K time-dependent compressive deformation of single-crystalline and polycrystalline B2 Ni-40Al, Metal. Trans. 22A (1991) 1595–1607.

[24] S.V. Raj, S.C. Farmer, Characteristics of a new creep regime in polycrystalline NiAl, Metall. Mater. Trans. 26A (1995) 343–356.

[25] R.S. Sundar, S.C. Deevi, High-temperature strength and creep resistance of FeAl, Mater. Sci. Eng. A357 (2003) 124–133, https://doi.org/10.1016/S0921-5093(03)00261-2.

[26] S.M. Oppenheimer, A.R. Yung, D.C. Dunand, Power-law creep in near-equiatomic nickel–titanium alloys, Scripta Mater. 57 (2007) 377–380, https://doi.org/10.1016/j.scriptamat.2007.05.004.

[27] L. Reimer, Transmission Electron Microscopy Physics of Image Formation and Microanalysis, Springer, Berlin Heidelberg, 1993.

[28] R. K Ham, The determination of dislocation densities in thin films, Phil. Mag. 6 (1961) 1183–1184, https://doi.org/10.1080/14786436108239679.

[29] W. Blum, J. Dvořák, P. Král, M. Petrenec, P. Eisenlohr, V. Sklenička, In situ study of microstructure and strength of severely predeformed pure Cu in deformation at 573 K, Phil. Mag. 95 (2015) (2015) 3696–3711, https://doi.org/10.1080/14786435.2015.1096025.

[30] F. Dobeš, O. Zvěřina, J. Čadek, Loading system for creep tests at constant compressive stress, Kov. Mat. 5 (1986) 599–610.

[31] J.D. Whittenberger, R.D. Noebe, Elevated temperature compressive properties of Zr-modified NiAl, Metall. Mater. Trans. 27A (1996) 2628–2641.

[32] A.K. Yadav, D. Singh, S. Tripathi, V. Bhalla, R.R. Yadav, Temperature dependent elastic and ultrasonic properties of iron aluminide, Univ. J. Mater. Sci. 2 (2013) 56–62, https://doi.org/10.13189/ujms.2013.010208.

[33] R.V. Nandedkar, P. Delavignette, On the formation of a new superstructure in the zirconium-aluminium system, Phys. Status Solidi 73A (1982) 157–160, https://doi.org/10.1002/pssa.2210730246.

[34] P.J. Brown, J.B. Forsyth, The structure of the σ-phase Nb$_2$A1, Acta Crystallogr. 14 (1961) 362–364.

[35] B. Schuh, F. Mendez-Martin, B. Völker, E.P. George, H. Clemens, R. Pippan, A. Hohenwarter, Mechanical properties, microstructure and thermal stability of a nanocrystalline CoCrFeMnNi high-entropy alloy after severe plastic deformation, Acta Mater. 96 (2015) 258–268, https://doi.org/10.1016/j.actamat.2015.06.025.

[36] F. Otto, A. Dlouhý, K.G. Pradeep, M. Kuběnová, D. Raabe, G. Eggeler, E.P. George, Decomposition of the single-phase high-entropy alloy CrMnFeCoNi after prolonged anneals at intermediate temperatures, Acta Mater. 112 (2016) 40–52, https://doi.org/10.1016/j.actamat.2016.04.005.

[37] B. Schuh, B. Völker, J. Todt, N. Schell, L. Perriere, J. Li, J.P. Couzinié, A. Hohenwarter, Thermodynamic instability of a nanocrystalline, single-phase TiZrNbHfTa alloy and its impact on the mechanical properties, Acta Mater. 142 (2017) 201–212, https://doi.org/10.1016/j.actamat.2017.09.035.

[38] B. Schuh, B. Völker, V. Maier-Kiener, J. Todt, J. Li, A. Hohenwarter, Phase decomposition of a single-phase AlTiVNb high-entropy alloy after severe plastic deformation and annealing, Adv. Eng. Mater. 19 (2017) 1600674, https://doi.org/10.1002/adem.201600674.

[39] J.Y. He, H. Wang, Y. Wu, X.J. Liu, T.G. Nieh, Z.P. Lu, High-temperature plastic flow of a precipitation-hardened FeCoNiCr high entropy alloy, Mater. Sci. Eng. A 686 (2017) 34–40, https://doi.org/10.1016/j.msea.2017.01.027.

[40] J.Y. He, C. Zhu, D.Q. Zhou, W.H. Liu, T.G. Nieh, Z.P. Lu, Steady state flow of the FeCoNiCrMn high entropy alloy at elevated temperatures, Intermetallics 55 (2014) 9–14, https://doi.org/10.1016/j.intermet.2014.06.015.

[41] Y.B. Kang, S.H. Shim, K.H. Lee, S.I. Hong, Dislocation creep of CoCrFeMnNi high entropy alloy at intermediate temperatures, Mater. Res. Lett. 6 (2018) 689–695, https://doi.org/10.1080/21663831.2018.1543731.

[42] J. Cadek, Creep in Metallic Materials, Elsevier Science Publishers, Amsterdam, 1988.

[43] I. Poschmann, H.J. McQueen, Flow softening and microstructural evolution of Al-5Mg during hot working, Scripta Mater. 35 (1996) 1123–1128, https://doi.org/10.1016/1359-6462(96)00285-0.

[44] D.G. Morris, M.A. Morris, Dislocation processes leading to the stress anomaly in B2-type Fe-40%Al single crystals, Intermetallics 5 (1997) 245–263, https://doi.org/10.1016/S0966-9795(96)00095-7.

[45] W. Blum, E. Weckert, On the interpretation of the "Internal stress" determined from dip tests during creep of Al-5at.%Mg, Mater. Sci. Eng. 86 (1987) 145–158, https://doi.org/10.1016/0025-5416(87)90449-6.

[46] E. Weckert, W. Blum, Transient creep of an Al-5at%Mg solid solution, in: Proceedings of the 7th International Conference on the Strength of Metals and Alloys, Montreal, Canada, 1985, pp. 773–777, https://doi.org/10.1016/B978-0-08-031642-0.50135-5.